catalysts

MDPI

Article

Segregation of Nickel/Iron Bimetallic Particles from Lanthanum Doped Strontium Titanates to Improve Sulfur Stability of Solid Oxide Fuel Cell Anodes

Patrick Steiger [1,2], Dariusz Burnat [3], Oliver Kröcher [1,2], Andre Heel [3] and Davide Ferri [1,*]

1 Paul Scherrer Institut, Forschungsstrasse 111, CH-5232 Villigen, Switzerland; patrick.steiger@psi.ch (P.S.); oliver.kroecher@psi.ch (O.K.)
2 École Polytechnique Fédérale de Lausanne (EPFL), Institute of Chemical Sciences and Engineering, CH-1015 Lausanne, Switzerland
3 Zurich University of Applied Sciences, IMPE – Institute for Materials and Process Engineering, CH-8400 Winterthur, Switzerland; dariuszartur.burnat@zhaw.ch (D.B.); andre.heel@zhaw.ch (A.H.)
* Correspondance: davide.ferri@psi.ch; Tel.: +41-56-310-2781

Received: 19 March 2019; Accepted: 1 April 2019; Published: 3 April 2019

Abstract: Perovskite derived Ni catalysts offer the remarkable benefit of regeneration after catalyst poisoning or Ni particle growth through the reversible segregation of Ni from the perovskite-type oxide host. Although this property allows for repeated catalyst regeneration, improving Ni catalyst stability towards sulfur poisoning by H_2S is highly critical in solid oxide fuel cells. In this work Mn, Mo, Cr and Fe were combined with Ni at the B-site of $La_{0.3}Sr_{0.55}TiO_{3\pm\delta}$ to explore possible benefits of segregation of two transition metals towards sulfur tolerance. Catalytic activity tests towards the water gas shift reaction were carried out to evaluate the effect of the additional metal on the catalytic activity and sulfur stability of the Ni catalyst. The addition of Fe to the Ni perovskite catalyst was found to increase sulfur tolerance. The simultaneous segregation of Fe and Ni from $La_{0.3}Sr_{0.55}Ti_{0.95-x}Ni_{0.05}Fe_xO_{3\pm\delta}$ ($x \leq 0.05$) was investigated by temperature programmed reduction, X-ray diffraction and X-ray absorption spectroscopy and catalytic tests after multiple redox cycles. It is shown that catalytic properties of the active phase were affected likely by the segregation of Ni/Fe alloy particles and that the reversible segregation of Ni persisted, while it was limited in the case of Fe under the same conditions.

Keywords: nickel; $La_{0.3}Sr_{0.55}Ti_{0.95}Ni_{0.05}O_{3\pm\delta}$; catalyst regeneration; structural reversibility; H_2S; solid oxide fuel cell

1. Introduction

In recent years perovskite-type metal oxide (PMO) derived metal catalysts have attracted great attention for their high redox stability, due to the reversible segregation of catalytically active metals from the bulk of the oxide in reducing atmospheres and their reincorporation during oxidative treatments [1]. It was demonstrated that this property allows for the regeneration of catalysts, which have suffered from active metal particle sintering, as well as the recovery of catalysts poisoned by coke or sulfur through simple redox cycling [2,3]. However, achieving catalyst stability while maintaining high catalytic conversion rates, thus decreasing the necessary frequency of catalyst regeneration cycles, appears to be as propitious as increasing catalyst regenerability. This is especially important in redox-sensitive electrochemical devices, such as solid oxide fuel cells (SOFCs), where metallic Ni is typically applied as the active phase in the anode for fuel oxidation, but also for its activity towards the water gas shift reaction (WGS) when the device is operated on CO-rich feeds [4,5]. Prominent examples of sulfur poisoning in heterogeneous catalysis include exhaust gas after-treatment reactions in the

three-way catalytic converters and the selective catalytic reduction of NO_x compounds [6], methanation of carbon oxides [7], reforming of methane and higher hydrocarbons [8,9], Fischer-Tropsch [10] and methanol synthesis from syngas [11]. In the case of all metal-catalyzed reactions, sulfur tolerance may generally be increased in three ways: (i) Increasing the number of catalytically active sites, which leaves higher number of free active sites at equal sulfur surface coverage, (ii) a sacrificial species may be introduced on the catalyst, which preferentially interacts with sulfur leaving the active species available for the reaction and (iii) the electronic effect on the active metal caused by the introduction of a second metal may result in decreased metal-sulfur interactions [12]. In the case of the Ni-catalyzed WGS reaction, promising results have been reported regarding improved sulfur stability of Ni reforming catalysts by the addition of Mo, Co and Re [13]. The beneficial effect of Re was attributed to the formation of a sulfur tolerant alloy, whereas in Ni-Mo metal combinations Mo acted as the sacrificial element [14]. The interaction between Ni and Mo was found to also increase the electron density on Mo thus facilitating its interaction strength with electronegative sulfur. Re-doping was also applied to improve sulfur tolerance of a Ni-Sr/ZrO_2 catalyst for the reforming of hydrocarbons [15]. Metal-metal interactions were also exploited to reduce the electron donor capacity of Pd by Mn addition thus decreasing its interaction strength with sulfur [16–18]. It is likely that doping of the Ni phase with other transition metals may also change sulfur adsorption properties on Ni.

It is the aim of the present work to combine the excellent regenerability of PMO-derived Ni catalysts for the WGS reaction with the possibility to alter the adsorption properties by transition metal doping of $La_{0.3}Sr_{0.55}Ti_{0.95}Ni_{0.05}O_{3\pm\delta}$, a self-regenerable SOFC anode material [2]. Sulfur sensitive elements, such as Cr, Mn, Fe and Mo were selected as potential sacrificial agents for screening towards a Ni-metal combination resistant to sulfur. Molybdenum, Cr and Mn are also of great importance to industrial high-temperature WGS catalysts [19].

2. Results

The work is structured as follows. We start showing the characterization of all materials (Table S1 for sample denotation) using ex situ and in situ X-ray diffraction (XRD) and temperature programmed reduction (TPR). Then the catalytic activity of the materials towards the water gas shift reaction (WGS) in the absence and presence of H_2S is presented. Because $La_{0.3}Sr_{0.55}Ti_{0.95}Ni_{0.05}O_{3\pm\delta}$ impregnated by Fe resulted in the most promising in terms of sulfur uptake and resistance to poisoning, further samples were prepared with various Fe/Ni ratios (see Materials and Methods and Table 1 for sample denotation), which were characterized also for the local environment of Ni and Fe using X-ray absorption spectroscopy and were tested for reaction and poisoning.

2.1. Characterization

Figure 1 shows X-ray diffraction (XRD) patterns of the materials after impregnation of $La_{0.3}Sr_{0.55}TiO_{3\pm\delta}$ (LST) and $La_{0.3}Sr_{0.55}Ti_{0.95}Ni_{0.05}O_{3\pm\delta}$ (LSTN) with the metal precursors and subsequent calcination. XRD patterns are also given for LST (Figure 1a) and LSTN (Figure 1b). The reflections of the corresponding single metal oxides were observed in the XRD patterns of impregnated LST (LST-5Me, Me = Cr, Mn, Fe and Ni; Figure 1c), as well as impregnated LSTN (LSTN-5Me, Me = Cr, Mn and Fe; Figure 1d). Impregnation with the Mo precursor (LST-5Mo and LSTN-5Mo) resulted in the presence of reflections of a $SrMoO_4$ phase, which is indicative of the segregation of small quantities of Sr from both LST and LSTN lattices during impregnation and calcination.

TPR experiments revealed the reduction of MnO, Cr_2O_3, Fe_2O_3 and NiO on LST up to 800 °C (Figure 2a). $SrMoO_4$ was only partially reduced at these temperatures as is evident from the fact that H_2 was still consumed at 800 °C. Similar behavior was also observed on impregnated LSTN materials (Figure 2c), on which also contributions of the LSTN support can be observed between ca. 450 °C and 650 °C. XRD measurements of the reduced materials confirmed the reduction of NiO, Fe_2O_3 and partial reduction of $SrMoO_4$ on LST-5Ni, LST-5Fe and LST-5Mo, respectively (Figure 2b). No reflections of Cr and Mn metals were observed on reduced LST-5Cr and LST-5Mn, respectively. Instead, reflections

of the single oxides were observed, similar to the calcined materials. This was likely due to the ex situ nature of the XRD experiments and the strong tendency of dispersed Cr and Mn particles to form oxides.

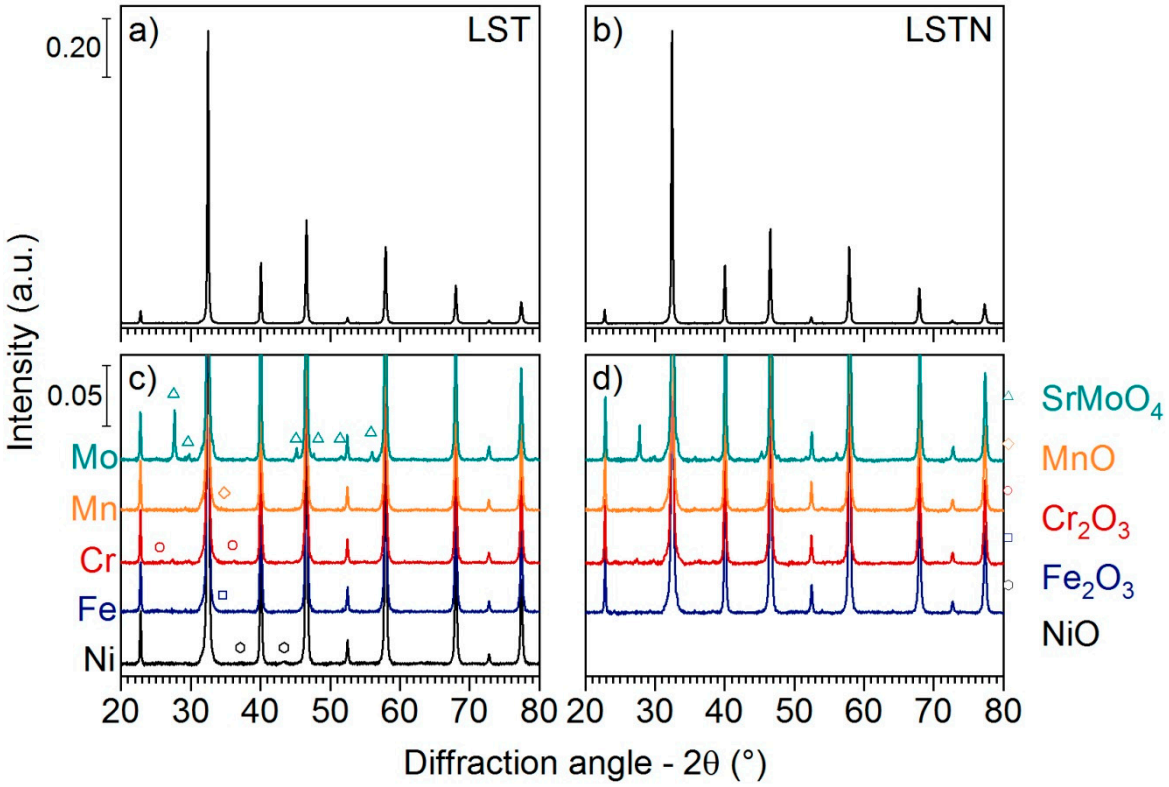

Figure 1. Powder XRD patterns of (**a**) $La_{0.3}Sr_{0.55}TiO_{3\pm\delta}$ (LST), (**b**) $La_{0.3}Sr_{0.55}Ti_{0.95}Ni_{0.05}O_{3\pm\delta}$ (LSTN), (**c**) LST-5Me (Me = Mo, Mn, Cr, Fe, Ni) and (**d**) LSTN-5Me (Me = Mo, Mn, Cr and Fe). Markers indicate the presence of metal oxide phases after impregnation. Note that the intensity of the diffractograms in (**c**) and (**d**) is magnified (5×) with respect to (**a**) and (**b**).

All reflections were also encountered on the reduced LSTN-type materials. However, reduced LSTN-5Fe exhibited reflections that indicated the presence of two Fe allotropes (α-Fe and γ-Fe, Figure 2d), which is likely a consequence of Fe/Ni alloy formation during reduction at 800 °C as it was not observed on LST-5Fe. Subsequent rapid cooling to room temperature after reduction resulted in phase separation. This is supported by phase diagrams of the Fe-Ni system, which predict partial phase decomposition of the homogeneous γ-Fe/Ni alloy phase and various phase transformations during cooling [20]. Since cooling rates were high in these experiments (ca. 20 °C·min^{-1}) the presence of metallic phases, which are not at equilibrium is highly probable [21]. Ni (111) reflections could be observed in LSTN, LSTN-5Cr and LSTN-5Mn, whereas the absence of the same in LSTN-5Fe and LSTN-5Mo can be regarded as an indication of Ni/Me alloy formation in the latter cases.

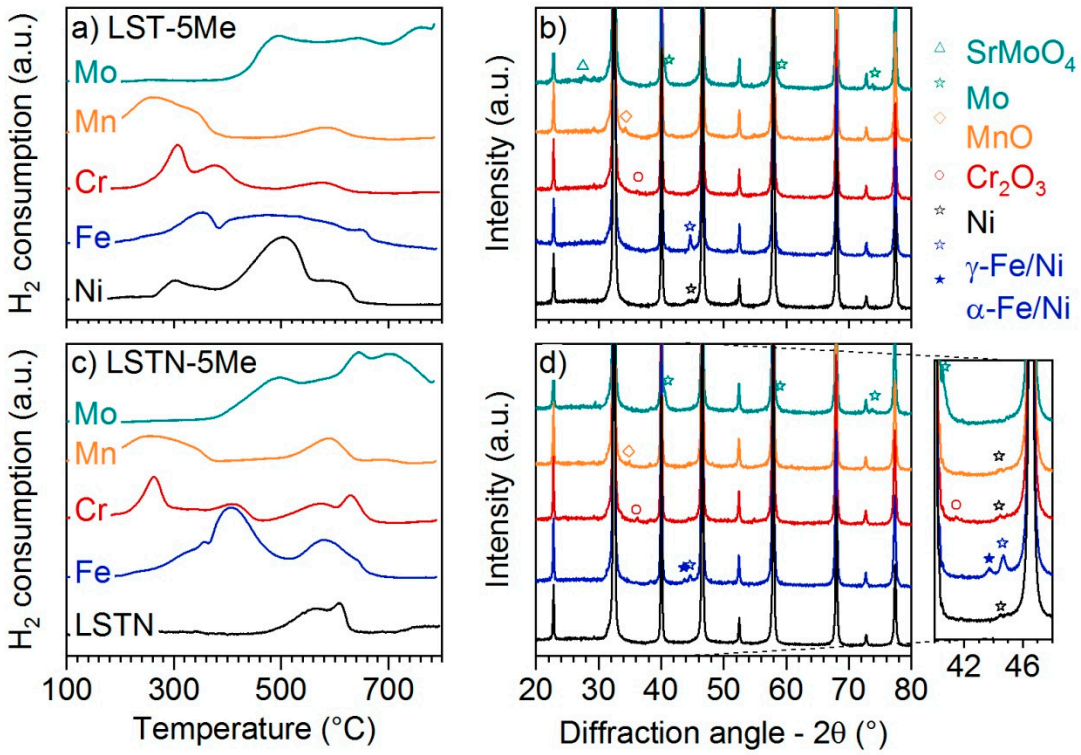

Figure 2. TPR profiles of (**a**) LST-5Me (Me = Mo, Mn, Cr, Fe, Ni) and (**c**) LSTN-5Me (Me = Mo, Mn, Cr, Fe). (**b**) Powder XRD patterns of reduced LST-type materials and (**d**) LSTN-type materials (10 vol.% H_2/Ar, 800 °C, 1 h). The additional panel in (**d**) displays the magnified angular range $40° \leq 2\theta \leq 48°$ (3×) with respect to intensity.

2.2. Catalytic Activity

The activity of the pre-reduced catalysts towards the water gas shift (WGS) reaction was assessed by measuring CO conversion between 300 °C and 800 °C and the results are shown in Figure 3. Activities of the catalysts produced using Ni-free LST as a support are displayed in Figure 3a. Nickel was the most active among all metals and LST-5Ni exhibited CO conversion above 60% at 460 °C. The next best activities were shown by LST-5Fe followed by LST-5Mn and finally LST-5Mo and LST-5Cr, which showed only limited activities at reactions temperatures below 800 °C. The lack of activity of Cr and Mo is not surprising. Molybdenum was added with the specific intent to introduce an element with negligible WGS activity, but with significant sensitivity to sulfur to be used as a sacrificial agent. Chromium is mainly used in Fe/Cr-based WGS catalysts for its capability to stabilize the active Fe phase [22]. Since LST did not show any significant WGS activity (Figure 3a) it can be assumed that the catalytic activity of LST-Ni, LST-Fe and LST-Mn was due to the impregnated metal. The CO conversion of each catalyst after poisoning is shown by the dashed lines in Figure 3a. Only LST-5Ni suffered severely during catalyst poisoning using 50 ppm H_2S under reaction conditions (800 °C, 1 h). The catalytic activity of LST-5Fe, LST-5Mn, LST-5Cr and LST-5Mo on the other hand, remained rather constant.

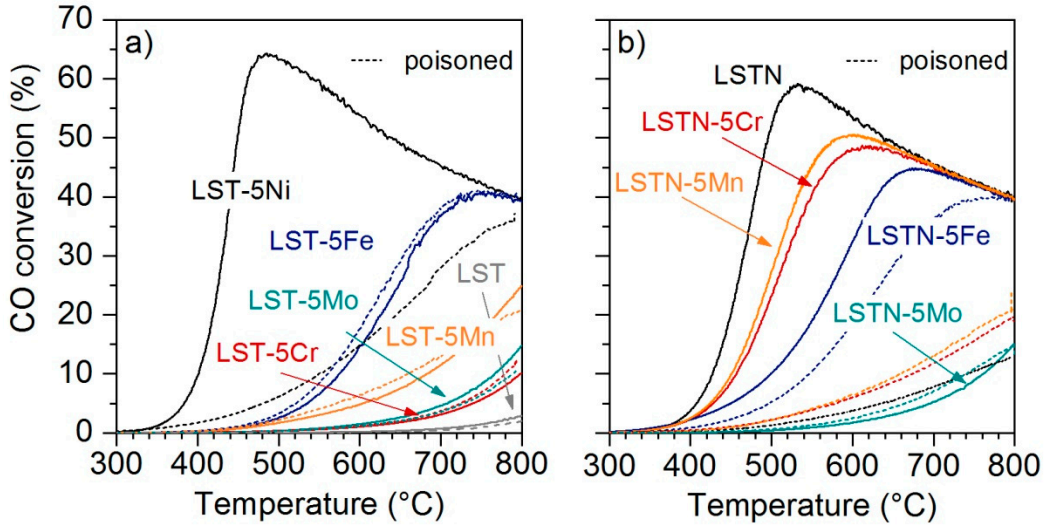

Figure 3. (**a**) WGS activity of LST impregnated with Cr (red), Fe (blue), Mn (orange), Mo (turquoise) and Ni (black) before (continuous lines) and after (dotted lines) catalyst poisoning with 50 ppm H_2S. (**b**) WGS activity of LSTN (black), as well as LSTN impregnated with Cr (red), Fe (blue), Mn (orange) and Mo (turquoise).

Catalytic activities of impregnated LSTN-type catalysts are displayed in Figure 3b. LSTN exhibited the highest activity towards the WGS reaction, followed by LSTN-5Mn and LSTN-5Cr. LSTN-5Fe also exhibited higher activity than its Ni-free counterpart LST-5Fe, whereas the low activity of LSTN-5Mo remained unchanged by the presence of Ni in the sample. The catalytic results provide an indication for Ni alloying with the impregnated metals Cr, Fe and Mn. The fact that all LSTN-5Me (Me = Cr, Fe, Mn, Mo) catalysts exhibited lower catalytic activity than LSTN, while all metals showed at least some activity towards WGS on Ni-free LST, provides evidence for close interaction between segregated Ni and Me in LSTN-5Me or coverage of the active Ni phase with the less active Me. This interaction was found to be less beneficial for WGS activity under sulfur-free conditions. However, catalytic tests after sulfur poisoning showed a stabilizing effect of the metals on WGS activity. Especially LSTN-5Fe was able to maintain comparably high levels of catalytic activity after poisoning by H_2S. It should be noted that the activity of LSTN-5Fe after poisoning did not exceed the one of LST-5Fe, which could indicate that Ni is still poisoned. Nevertheless, the improved activity of LSTN-5Fe in sulfur-free conditions compared to LST-5Fe demonstrates a potential benefit of a bimetallic catalyst.

2.3. Sulfur Uptake

Differences between the various materials were also observed in their behavior during H_2S adsorption. Figure 4a shows H_2S breakthrough curves for LST-5Me catalysts during sulfur loading. H_2S (50 ppm) was introduced to the reaction gas stream after 5 min equilibration time. Dosing H_2S over a blank quartz reactor resulted in negligible retention time and 50 ppm were attained after ca. 5 min. Sulfur adsorption can be observed by the increased retention times when H_2S is dosed over the catalyst bed. The longest retention time of around 8 min was recorded for LST-5Ni. The significant sulfur uptake of this sample (210 ppm by weight) is in line with its strong deactivation in terms of the catalytic activity after sulfur loading (Figure 3a). A retention time of around 4 min and 2 min was observed for LST-5Fe and LST-5Mn, respectively. H_2S breakthrough of LST-5Mo and LST-5Cr was close to the blank experiment indicating low sulfur adsorption properties of these metals. This indicates that the ability of Mo as a sulfur scavenger was limited on these samples compared to the more conventionally applied single oxides MoO_2 and MoO_3, possibly due to the $SrMoO_4$ phase formed during synthesis (Figure 1).

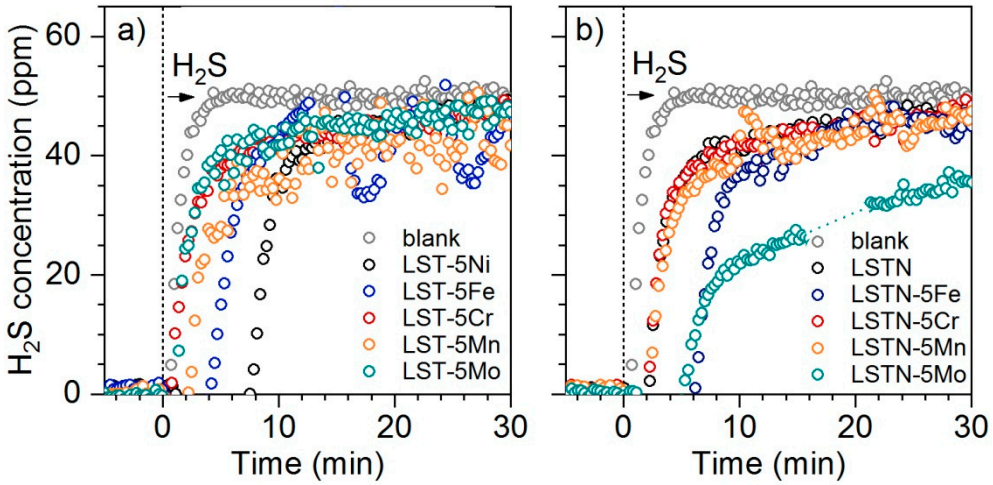

Figure 4. H_2S breakthrough curves during H_2S adsorption experiments on reduced (**a**) LST-5Me (Me = Mo, Mn, Cr, Fe, Ni) and (**b**) LSTN-5Me (Me = Mo, Mn, Cr and Fe). The start time of sulfur addition is indicated by the vertical dashed line.

Interestingly, LSTN-5Mo showed significant sulfur uptake exceeding the combined sulfur storage capabilities of LSTN and LST-5Mo. This can be regarded as an indication for close interaction between segregated Ni and Mo, which appeared to significantly change the sulfur uptake properties of the material. Retention times of LSTN-5Fe, LSTN-5Cr and LSTN-5Mo were approximately the sum of those of LSTN and their LST-5Me counterparts and can be therefore explained by the increased metal content on the sample surface. Sulfur uptake of LSTN was much lower than that of LST-5Ni (ca. 40 ppm compared to 210 ppm), which can be justified using the similar argumentation that when Ni is deposited on LST by impregnation, the Ni metal surface is higher compared to pre-reduced LSTN, due to partial Ni reduction in the latter. Although no obvious advantage of metal impregnation on LSTN could be observed from these H_2S adsorption experiments because none of the metals reduced the H_2S uptake of the sample, the increased sulfur tolerance in terms of the catalytic activity towards WGS exhibited by LSTN-5Fe (Figure 3b) could be an advantageous property. Therefore, the question arises whether it is possible to exploit the reversible segregation of metals from an LST-type host to produce both redox stable, as well as sulfur tolerant Ni/Fe catalysts.

2.4. $La_{0.3}Sr_{0.55}Ti_{1-x-y}Fe_xNi_yO_{3\pm\delta}$ (x = 0, 0.025, 0.05; y = 0, 0.05)

Catalytic activity and sulfur uptake data indicated that Fe might be a suitable candidate to improve sulfur tolerance of LSTN while maintaining the self-regeneration property. In order to explore the potential segregation of both Fe and Ni from the perovskite-type host, both Ni and Fe were introduced at the perovskite B-site of LST to obtain compositions of the type $La_{0.3}Sr_{0.55}Ti_{1-x-y}Fe_xNi_yO_{3\pm\delta}$ (x = 0, 0.025, 0.05; y = 0, 0.05) the denotations of which are summarized in Table 1. Figure 5 displays a summary of XRD patterns collected on calcined materials, as well as after 15 h reduction at 800 °C (10 vol.% H_2/Ar).

All calcined samples exhibited only reflections, which could be attributed to the perovskite host. After reduction, weak reflections belonging to metallic phases were observed. Reduced $La_{0.3}Sr_{0.55}Ti_{0.95}Ni_{0.05}O_{3\pm\delta}$ (LSTN-5Ni) showed a reflection centered at 44.40°, which corresponds to the Ni (111) reflection. Reduced $La_{0.3}Sr_{0.55}Ti_{0.925}Fe_{0.025}Ni_{0.05}O_{3\pm\delta}$ (LSTFN-2Fe5Ni) and $La_{0.3}Sr_{0.55}Ti_{0.9}Fe_{0.05}Ni_{0.05}O_{3\pm\delta}$ (LSTFN-2Fe5Ni) exhibited a weak reflection at 43.77°, which is higher than one would expect for the (111) reflection of metallic Fe (43.6° 2θ), but certainly at lower angles than the Ni (111) reflection. This can be regarded as evidence for Ni/Fe alloy particle formation upon reduction of LSTFN-type materials. $La_{0.3}Sr_{0.55}Ti_{0.925}Fe_{0.025}Ni_{0.05}O_{3\pm\delta}$ (LSTF-5Fe) did not show significant reflections of metallic Fe after reduction. However, a new reflection appeared at 38.27°,

which could not be assigned to any metallic phase. While metallic Ti is expected to display a reflection at around 38.4°, it is highly unlikely that it formed under these pretreatment conditions, due to the inherent stability of Ti^{4+}. The missing reflection at 35.2° excludes this possibility conclusively. However, the observed reflection could be explained by the formation of a new perovskite-type phase of lower symmetry. Orthorhombic perovskites (such as A-site stoichiometric $LaSrFeO_{3\pm\delta}$) possess a reflection at ca. 38° corresponding to the (113) lattice planes. All other reflections might be either hidden below the dominant original perovskite phase or too weak to be observed.

Table 1. Sample denotations and metal content of $La_{0.3}Sr_{0.55}Ti_{1-x-y}Fe_xNi_yO_{3\pm\delta}$ -type samples.

Denotation	Formula	Ni Content (mol.%)	Fe Content (mol.%)
LSTN-5Ni	$La_{0.3}Sr_{0.55}Ti_{0.95}Ni_{0.05}O_{3\pm\delta}$	5	0
LSTFN-2Fe5Ni	$La_{0.3}Sr_{0.55}Ti_{0.925}Fe_{0.025}Ni_{0.05}O_{3\pm\delta}$	5	2.5
LSTFN-5Fe5Ni	$La_{0.3}Sr_{0.55}Ti_{0.9}Fe_{0.05}Ni_{0.05}O_{3\pm\delta}$	5	5
LSTF-5Fe	$La_{0.3}Sr_{0.55}Ti_{0.95}Fe_{0.05}O_{3\pm\delta}$	0	5

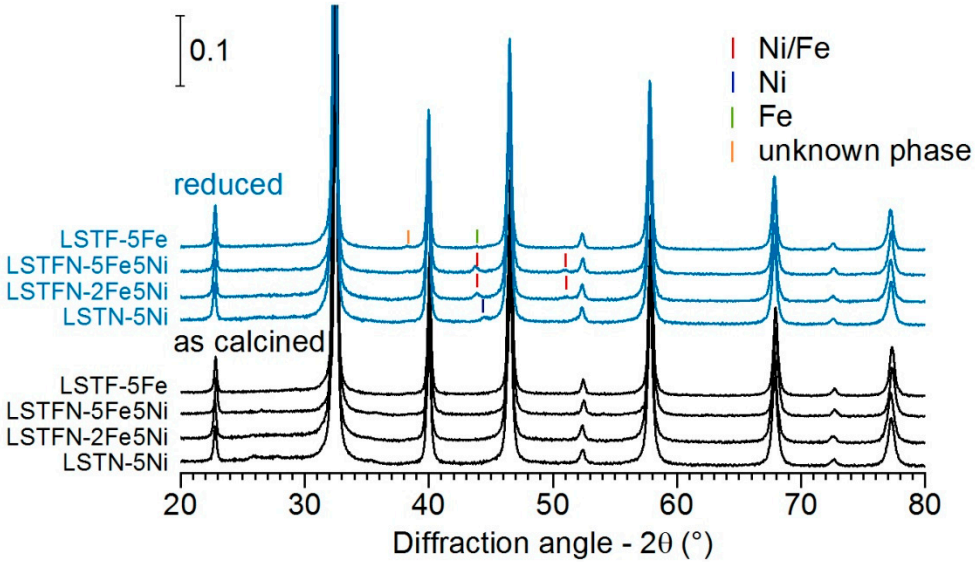

Figure 5. Powder XRD patterns of calcined and reduced LSTN-5Ni, LSTFN-2Fe5Ni, LSTFN-5Fe5Ni and LSTF-5Fe (10 vol.% H_2/Ar, 800 °C, 15 h). Diffractograms are magnified with respect to intensity (2×) to emphasize Ni, Fe and Ni/Fe reflections.

The materials were subjected to TPR and reoxidation cycles to verify the structural reversibility and to determine the temperature at which segregated metals are reversibly incorporated into the host perovskite lattice. In these experiments, TPR profiles were followed by an isothermal reduction at 800 °C. The materials were then subsequently reoxidised at the indicated temperature (700 °C, 750 °C, 800 °C, 850 °C, 900 °C and 950 °C) before the next TPR profile was collected. The TPR profile is sensitive to the nature and coordination environment of reducible metal species and such experiments can, therefore, be exploited to determine the reoxidation temperature needed to reestablish the state of the reducible metal species in the initial calcined material [2,23]. Figure 6a displays the TPR redox cycles obtained on LSTN-5Ni. The reduction feature of NiO (ca. 370 °C) disappears after reoxidation at $T_{reox} \geq 800$ °C, thus indicating successful and complete Ni reincorporation at this temperature [2]. The initial TPR of calcined LSTFN-2Fe5Ni (Figure 6b) was not as well defined as the one recorded for LSTN-5Ni. Instead of the distinct double feature, the sample exhibited a broad reduction peak between 400 °C and 650 °C. After reduction and subsequent reoxidation at low temperatures (700 °C and 750 °C) the sample exhibited a low temperature feature peaking at around 475 °C. This feature then

transitioned into the previously observed double feature for reoxidation above 850 °C, which could be interpreted as the temperature at which both Fe and Ni are reincorporated into the perovskite host.

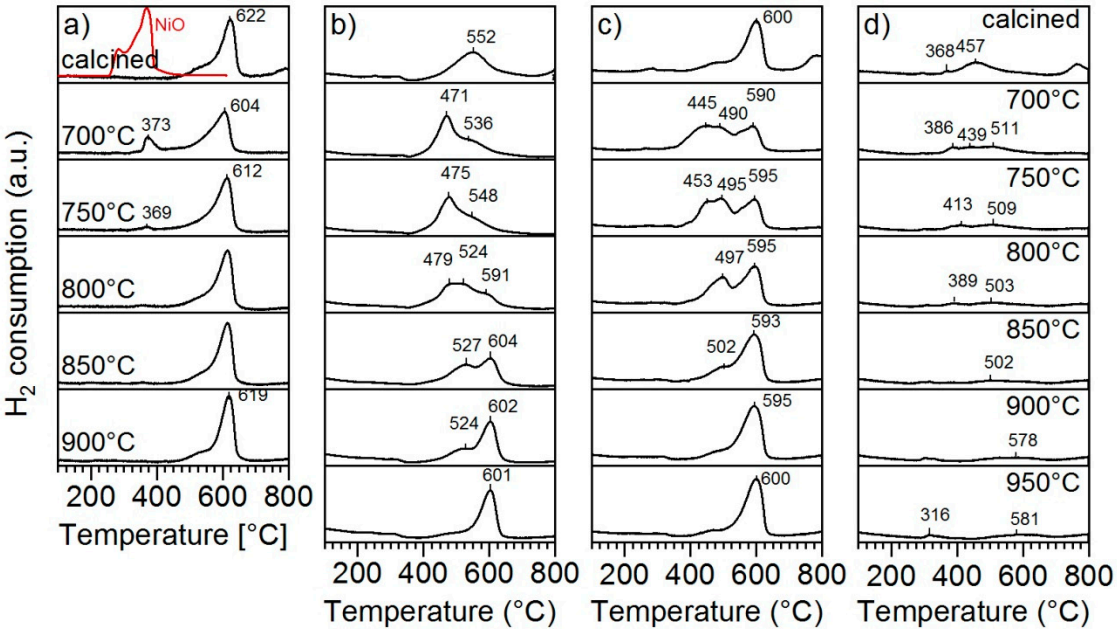

Figure 6. TPR reduction-reoxidation cycles for (**a**) LSTN, (**b**) LSTFN-2Fe5Ni, (**c**) LSTFN-5Fe5Ni and (**d**) LSTF-5Fe. Hydrogen consumption values were normalized by molar quantity of sample. Reoxidized samples were subjected to pre-reduction (10 vol.% H_2/Ar, 800 °C, 1 h) before reoxidation (20 vol.% O_2/N_2, 2 h) at the temperature indicated for each row.

The sample with higher Fe content (LSTFN-5Fe5Ni; Figure 6c) exhibited the reduction feature, which was attributed previously to a two-step reduction process of Ni [24]. However, peak reduction temperatures were shifted to lower temperatures by 22 °C compared to the ones recorded for LSTN-5Ni in Figure 6a. Reoxidation at lower temperatures caused the formation of a new reduction feature between 350 °C and 550 °C also on this sample, which can be attributed to the reoxidation of Ni/Fe oxides at the perovskite surface. Reestablishment of the initial reduction profile was achieved after reoxidation at 850 °C. Interestingly, LSTF-5Fe (Figure 6d) did not exhibit as an extensive reduction as the other samples; the reduction features were broad and attenuated with increasing reoxidation temperature. In this case, TPR-redox cycling seemed unsuitable to accurately trace the reoxidation temperature necessary for Fe reincorporation and demonstrates the limited reducibility of Fe in LSTF-5Fe in absence of Ni.

Even though TPR provides important insight in the reducibility of the materials, only an element specific method, such as X-ray absorption spectroscopy (XAS) can be used to ultimately differentiate between individual contributions of two or more reducible species. Therefore, XAS was applied to investigate the effect of the simultaneous presence of both Fe and Ni in LSTFN-type samples on the reduction and reoxidation of the individual metals. Figure 7 displays the Ni K-edge (8.333 keV) X-ray absorption near edge structure (XANES) spectra of the Ni-containing samples LSTN-5Ni (Figure 7a), LSTFN-2Fe5Ni (Figure 7b) and LSTFN-5Fe5Ni (Figure 7c) in their calcined state, as well as after reduction (10 vol.% H_2/Ar, 800 °C, 15 h) and reoxidation (20 vol.% O_2/N_2, 800 °C, 2 h).

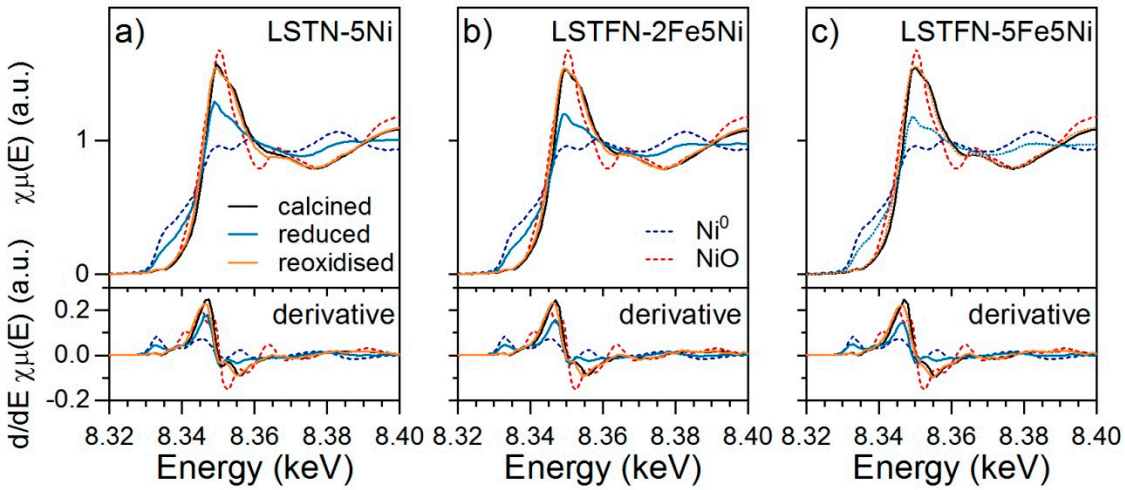

Figure 7. Normalized Ni K-edge (8.333 keV) XANES spectra of (**a**) calcined and reduced (10 vol.% H_2/Ar, 800 °C, 15 h) LSTN-5Ni, (**b**) LSTFN-2Fe5Ni and (**c**) LSTFN-5Fe5Ni. Plots of the first derivative of the normalized spectra are shown in the bottom panels. The spectra of Ni foil and NiO reference materials are included for comparison (dashed lines).

The Ni K-edge spectra of the calcined materials displayed an intense whiteline with a high energy shoulder that can be taken as characteristic of Ni adopting the coordination environment of Ti [2,25,26]. The edge energy was also higher than in the case of Ni^{2+} in NiO. After reduction, the spectra corresponded to a linear combination of the spectra of Ni adopting the coordination environment of the B-site after calcination and Ni^0. Although TPR analysis showed reversibility only after reoxidation at 850 °C (Figure 6), the shape of the XANES spectra and thus the state of Ni were completely reversible in this redox cycle, which was carried out at lower temperatures. It was also observed that the contribution of the Ni^0 reference to the spectra of the reduced samples increased with increasing Fe concentration. This was confirmed by linear combination fit (LCF) of the spectra indicating that the amount of Ni^0 increased from 52% in LSTN-5Ni to 62% in LSTFN-2Fe5Ni and to 67% in LSTFN-5Fe5Ni. LCF results are summarized in Figure S1 and the corresponding fit results are shown in Figure S2.

Evidence that Ni was not only reduced, but also segregated and formed metallic particles is provided by the extended X-ray absorption fine structure of the Ni K-edge. The k^3-weighted data is shown in Figure S3 for all samples, as well as Ni references. The radial distances of coordination shells become obvious through Fourier transformation of this data, as shown in Figure 8. After reduction, the feature attributed to a Ni-Ni coordination shell appeared at 2.15 Å. This feature was present for all samples so that metal particle formation can be assumed likewise.

Fe K-edge (7.112 keV) XANES data was obtained on the Fe-containing samples LSTFN-2Fe5Ni, LSTFN-5Fe5Ni and LSTF-5Fe and spectra of calcined, reduced and reoxidized samples are displayed in Figure 9 along with spectra of Fe^0, FeO, Fe_3O_4 and Fe_2O_3 reference compounds. Significant changes in the shape of the XANES could be observed also for Fe K-edge absorption spectra over the redox cycle. Clear Fe reduction could be observed by a decrease in whiteline intensity, as well as a shift in absorption edge energy (E_0). This shift is best determined through the position of the first maximum in the derivative of the absorption curves, which changes from 7.128 keV for calcined materials to 7.125 keV for reduced materials, corresponding to a decreased ionization energy, which is typically observed for reduced states. However, in the spectra of the reduced samples, the whiteline did not correspond to a simple linear combination of the reference spectrum of Fe^0 and the spectrum of calcined LSTFN- or LSTF-type materials, thus suggesting other states of Fe.

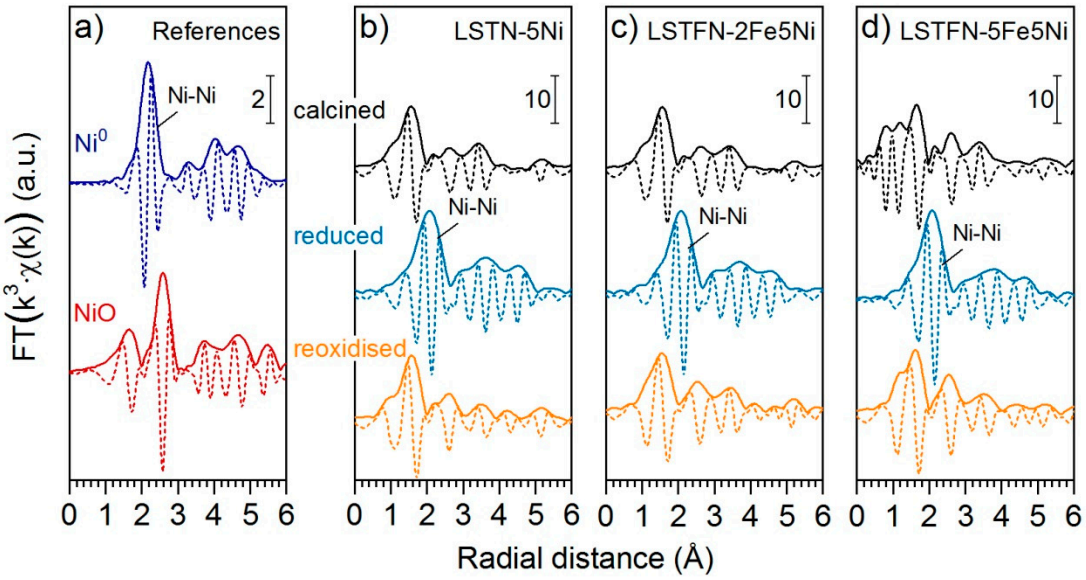

Figure 8. Fourier transformed k^3-weighted Ni K-edge EXAFS data obtained for (**a**) Ni^0 (Ni foil) and NiO reference materials, as well as calcined, reduced (10 vol.% H_2/Ar, 800 °C, 1 h) and reoxidized (20 vol.% O_2/N_2, 800 °C, 2 h) (**b**) LSTN-5Ni, (**c**) LSTFN-2Fe5Ni and (**d**) LSTFN-5Fe5Ni. Features are labelled on the reduced materials according to the underlying Ni-Ni scattering paths.

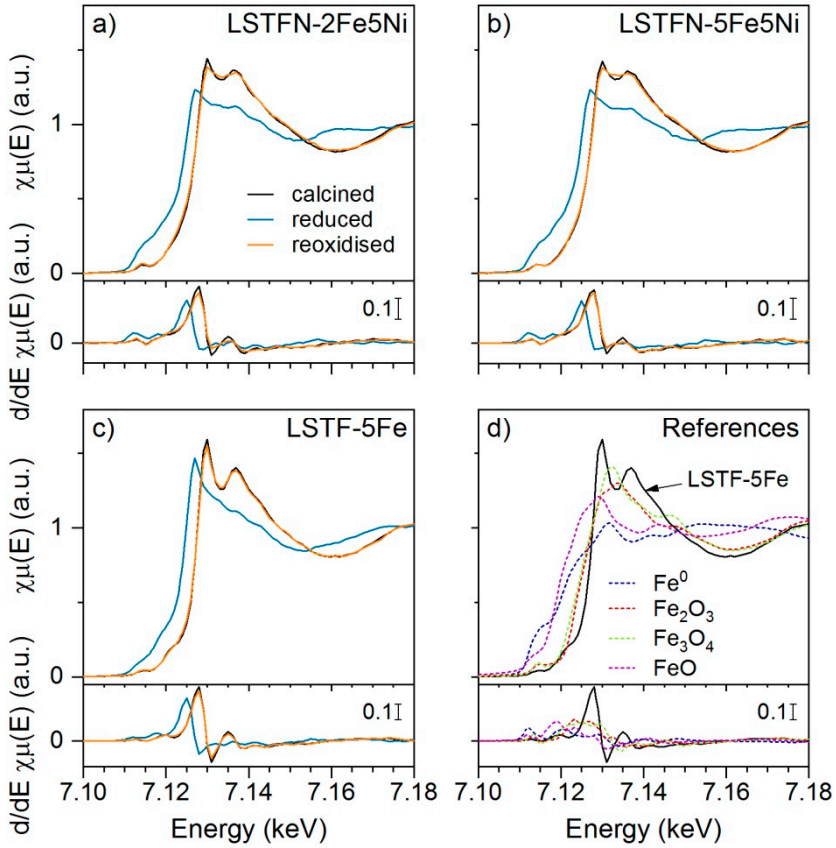

Figure 9. Normalized Fe K-edge (7.112 keV) XANES spectra of (**a**) calcined, reduced (800 °C, 10 vol.% H_2/Ar, 15 h) and reoxidized (800 °C, 20 vol.% O_2/N_2, 2 h) LSTFN-2Fe5Ni, (**b**) LSTFN-5Fe5Ni, (**c**) LSTF-5Fe. (**d**) XANES spectra of LST-5Fe, Fe^0, Fe_2O_3, Fe_3O_4 and FeO reference materials. The first derivative of the normalized spectra is shown in the bottom panels.

No suitable fits could be obtained through LCF analysis using all displayed Fe reference spectra. This may be linked to the presence of other Fe-containing phases as was already suggested from the XRD patterns in Figure 1. Furthermore, the XANES of LSTFN-2Fe5Ni and LSTFN-5Fe5Ni was not completely restored in the reoxidized materials as can be seen in the region of the local minimum at around 7.135 keV. LCF of the spectra of the reoxidized materials indicated the presence of Fe_3O_4 (ca. 17%) and thus incomplete reincorporation of Fe under the applied reoxidation conditions.

The k^3-weighted Fe K-edge (7.112 keV) EXAFS data of LSTFN-2Fe5Ni, LSTFN-5Fe5Ni and LSTF-5Fe is shown in Figure S4, whereas the Fourier transformed data is shown in Figure 10. Compared to the Ni^0 reference in Figure 8, Fe^0 in the Fe foil displayed the first coordination shell at a slightly longer radial distance (2.23 Å) and similar to the Ni K-edge data contributions of this feature, could be found in the spectra of the reduced samples. This indicates that besides Ni Fe was also partially reduced to Fe^0 and was present in the form of metal particles. Interestingly, the contribution of this feature to the spectra of the reduced samples decreased with decreasing Ni/Fe ratios along the series LSTFN-2Fe5Ni > LSTFN-5Fe5Ni > LSTF-5Fe, which suggests that larger Ni content favors Fe reduction. Hence, the positive influence of one metal on the reducibility and segregation of the other metal could be observed.

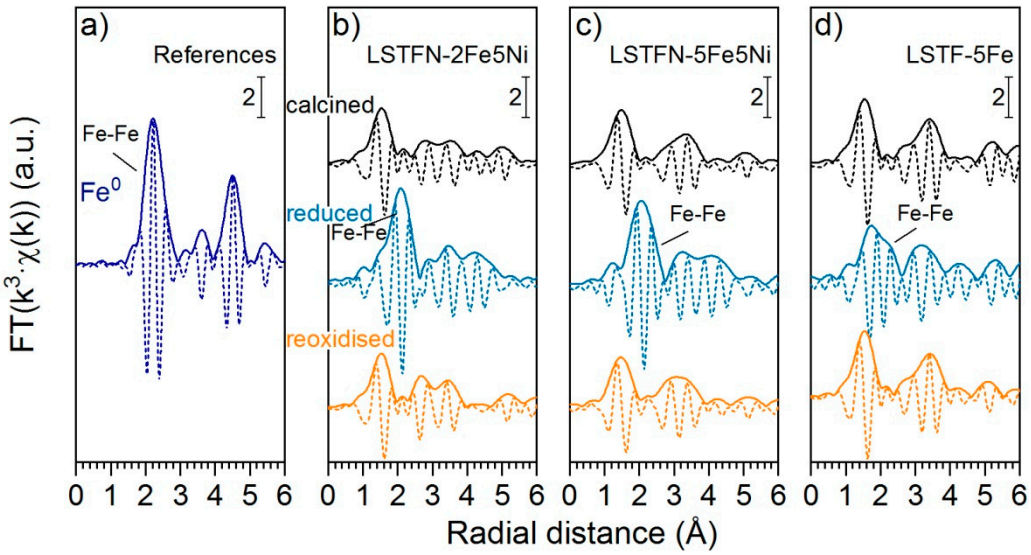

Figure 10. Fourier transformed k^3-weighted Fe K-edge EXAFS data obtained for (**a**) Fe^0 (Fe foil) reference, as well as (**b**) LSTFN-2Fe5Ni, (**c**) LSTFN-5Fe5Ni and (**d**) LSTF-5Fe after calcination, reduced (10 vol.% H_2/Ar, 800 °C, 1 h) and reoxidized (20 vol.% O_2/N_2, 800 °C, 2 h). Features are labelled on the reduced materials according to the underlying Fe-Fe scattering paths.

Figure 11a shows CO conversion curves for the Ni-containing samples LSTN-5Ni, LSTFN-2Fe5Ni and LSTFN-5Fe5Ni. It is apparent that the conversion curves shifted to higher temperatures with increasing Fe concentration, which corresponds to a decrease in catalytic activity. This is in contrast to the previous observation that the presence of Fe increases Ni reducibility (Figure S1). The expected effect would be a larger amount of active Ni^0 and thus higher catalytic activity. On the other hand, the observation is in line with the decrease in WGS activity observed for LSTN-5Fe compared to LSTN in Figure 3b and the indication of Ni/Fe alloy formation during reduction provided by this catalytic activity data, as well as XRD (Figure 5). Since the addition of small quantities of Fe did not appear to be detrimental for catalytic activity, LSTFN-2Fe5Ni was selected for testing catalytic activity with respect to its redox stability, as well as sulfur tolerance. However, it can be seen in Figure 11b that CO conversion decreased over the number of redox cycles, which could be a consequence of Ni/Fe particle growth, due to the incomplete Fe reincorporation over the redox cycles observed by XANES (Figure 9). Despite the fact that Ni re-incorporated completely during reoxidation of reduced

LSTFN-2Fe5Ni (Figure 7), the remaining Fe oxide at the surface may have caused particle growth and thus the observed catalyst deactivation over the consecutive redox cycles.

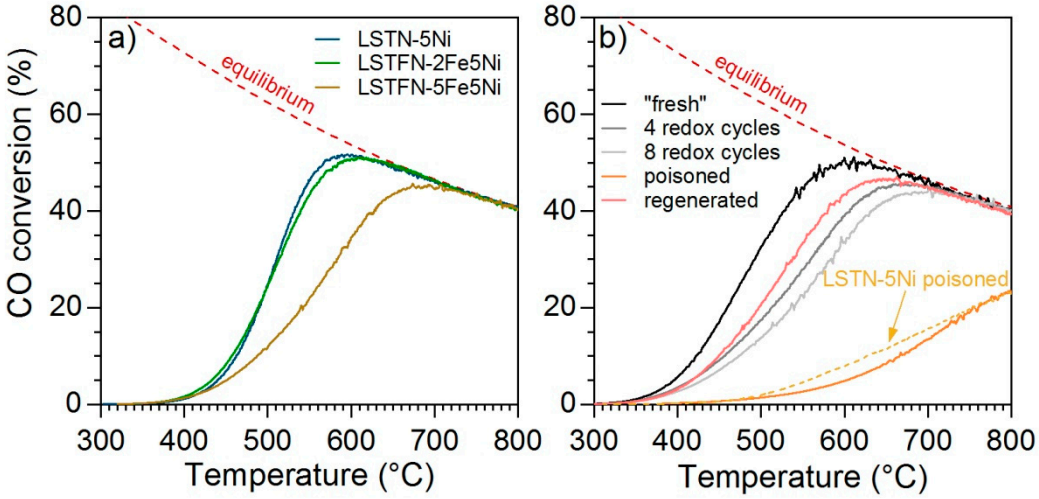

Figure 11. WGS activity of (**a**) reduced LSTN-5Ni, LSTFN-2Fe5Ni, LSTFN-5Fe5Ni (20 vol.% H_2/Ar, 800 °C, 15 h) and (**b**) LSTFN-2Fe5Ni after eight redox cycles, as well as after poisoning with 50 ppm H_2S under reaction conditions (poisoned) and after subjecting the material to one further redox cycle (regenerated). Feed gas composition: 15 vol.% CO/15 vol.% H_2O/7.5 vol.% H_2/Ar; 30,000 $mLh^{-1}g^{-1}$ at STP. The calculated theoretical conversion equilibrium is indicated by the dashed red curve.

The small amounts of Fe (2.5 mol.% or 0.75 wt.%) also did not provide additional stability against poisoning by sulfur, which can be realized from the CO conversion measured after catalyst poisoning by H_2S (Figure 11b). CO conversion was as low as in poisoned LSTN. A complete redox cycle recovered catalytic activity, which was even improved compared to the catalytic activity measured before poisoning. The reason behind this phenomenon was not further investigated as any obvious improvement in performance in terms of the catalytic activity of LSTFN-2Fe5Ni in neither sulfur-free nor sulfur-containing reaction gas feeds could be observed. Nevertheless, it indicates that sulfur can also be successfully removed from LSTFN-type oxides over oxidation-reduction cycles at 800 °C, which could be potentially exploited to completely regenerate these materials if catalyst redox stability can be achieved. The conditions to achieve full reversibility of activity after poisoning should be the aim of future work.

3. Materials and Methods

Mixed metal oxides with nominal composition $La_{0.3}Sr_{0.55}TiO_{3\pm\delta}$ (LST) and $La_{0.3}Sr_{0.55}Ti_{0.95}Ni_{0.05}O_{3\pm\delta}$ (LSTN) were synthesized according to the synthesis procedure described earlier and including a final calcination step at 960 °C (6 h) [27]. Aliquots of these two parent materials were then loaded with Fe, Cr, Mn and Mo precursors by wet impregnation with aqueous precursor solutions followed by drying at 120 °C for around 12 h and subsequent calcination at 500 °C for 2 h. Metal loading was chosen such that the final loading resembled the metal concentration in hypothetical $La_{0.3}Sr_{0.55}Ti_{0.95}Me_{0.05}O_{3\pm\delta}$ and $La_{0.3}Sr_{0.55}Ti_{0.9}Ni_{0.05}Me_{0.05}O_{3\pm\delta}$ (Me = Fe, Cr, Mn and Mo). Table S1 contains all information regarding type and quality of metal precursors used, as well as denotations of the corresponding samples, which are used throughout the text. Furthermore, $La_{0.3}Sr_{0.55}Ti_{0.925}Ni_{0.05}Fe_{0.025}O_{3\pm\delta}$ (LSTFN-2Fe5Ni), $La_{0.3}Sr_{0.55}Ti_{0.9}Ni_{0.05}Fe_{0.05}O_{3\pm\delta}$ (LSTFN-5Fe5Ni), $La_{0.3}Sr_{0.55}Ti_{0.95}Fe_{0.05}O_{3\pm\delta}$ (LSTF-5Fe), and $La_{0.3}Sr_{0.55}Ti_{0.95}Ni_{0.05}O_{3\pm\delta}$ (LSTN-5Ni) powders were also synthesized according to the same procedure, but were calcined at 860 °C for 6 h. After calcination, the powders are referred to as "calcined".

The catalytic activity towards the water gas shift (WGS) reaction was measured on powders in a quartz reactor of plug flow geometry (6 mm ID). Mass flow controllers (Brooks) were used to dose the reactant gases and a K-type thermocouple, which was placed in the middle of the catalyst bed, was used to monitor catalyst bed temperature. To avoid back pressure, all calcined powders were pelletized (4 MPa), crushed and sieved to 100−150 μm before use. The sample (100 mg) was diluted with cordierite powder (200 mg, 75−100 μm) to achieve a thoroughly mixed catalyst bed of ca. 15 mm in length. Catalytic tests were conducted on pre-reduced samples (20 vol.% H_2/Ar, 800 °C, 1 h) after an initial pretreatment of a single redox cycle. This treatment was found to activate LSTN [2] and has therefore been adopted in this work. Catalytic activities were measured at a weight hourly space velocity (WHGS) of 15,000 mL·g^{-1}·h^{-1} at STP (200 mg catalyst, 50 mL·min^{-1}). A Pfeiffer OmniStar GSD 320 quadrupole mass spectrometer equipped with a heated stainless steel capillary was used for compositional analysis of the exhaust gas. CO conversion (X_{CO}) was calculated using Equation (1),

$$X_{CO} = \frac{[CO]^{in} - [CO]^{out}}{[CO]^{in}} \times 100\% \quad (1)$$

where $[CO]^{in}$ is the initial concentration of CO and $[CO]^{out}$ is the concentrations of CO at the reactor outlet.

Sulfur loading of the catalyst samples was conducted under reaction conditions using the reaction gas mixture (15 vol.% H_2O/15 vol.% CO/7.5 vol.% H_2/Ar), including 50 ppm H_2S. Sulfur loading was conducted at 800 °C for 60 min during which H_2S concentration in the reactor exhaust was monitored using the mass spectrometer signal at M/Z = 34.

CO conversions of LSTN-5Ni, LSTFN-2Fe5Ni, LSTFN-5Fe5Ni were determined on powder samples after an initial activating redox cycle at WGHS= 30,000 mL·g^{-1}·h^{-1} (at STP).

The crystal structure of the powder catalysts was investigated by powder X-ray diffraction (XRD, Bruker D8 Advance) equipped with Ni-filtered Cu Kα-radiation, variable slits and an energy sensitive line detector (LynxEye). Diffractograms were collected at an acquisition time of 4 s and a step size of $\Delta 2\theta$ = 0.03° between 15° and 80°. Aliquots of the samples listed in Table S1 were reduced (10 vol.% H_2/Ar, 800 °C, 1 h) prior to XRD analysis. After reduction, samples were cooled down in Ar (20 °C·min^{-1}). XRD was also recorded on reduced samples at an increased resolution in the angular range 40°–50° (step size 0.005°). The XRD was also recorded for the Ni and Fe containing perovskite-type oxides LSTN-5Ni, LSTFN-2Fe5Ni, LSTFN-5Fe5Ni and LSTF-5Fe after prolonged reduction (10 vol.% H_2/Ar, 800 °C, 15 h).

Temperature programmed reduction (TPR) experiments were conducted using a bench top TPDRO-1100 (ThermoElectron) instrument equipped with mass flow controllers and a thermal conductivity detector. The samples (100 mg) were loaded into the quartz reactor tube and heated to 500 °C under a constant flow of 20 vol.% O_2 before cooling to room temperature. TPRs were recorded in 10 vol.% H_2/Ar (20 mL·min^{-1} at STP) and at a heating rate of 5 °C·min^{-1}. The reoxidation temperature at which Ni is reversibly reincorporated into the perovskite lattice was estimated by TPR redox experiments. A TPR profile was recorded on the calcined sample up to 800 °C followed by an isothermal reduction for 1 h at the same temperature. The sample was then cooled in Ar to room temperature (25 °C) before reoxidation at 700 °C in 20 vol.% O_2/N_2 for 2 h. The sample was again cooled in Ar to 25 °C before starting the second TPR on the now reoxidised material. Such TPR-reduction-reoxidation-TPR cycles were repeated five times with increasing reoxidation temperature (700 °C, 750 °C, 800 °C, 850 °C and 900 °C). The heating rate during reoxidation and cooling after all experiments was 10 °C·min^{-1}.

Ni K-edge (8.333 keV) and Fe K-edge (7.112 keV) X-ray absorption spectra were acquired ex situ on pelletized samples in fluorescence mode at the X10DA (SuperXAS) beamline of the Swiss Synchrotron Light Source (SLS, Villigen, Switzerland) using a 5 element SD detector. The required X-ray energies were scanned using a Si(111) monochromator. The Demeter software package (version

0.9.24) [28] was used to reduce and model all data. The radial distribution function (R) was obtained by Fourier transforming k^3-weighted k-functions typically in the range of 3.0−12.0 $Å^{-1}$ using a Hanning window function. NiO (99.99% trace metals basis, Sigma, Buchs, Switzerland), FeO (99.7% trace metal basis, Sigma), Fe_2O_3 (puriss. ≥97%, Sigma, Buchs, Switzerland), Fe_3O_4 (99.99% trace metal basis, Sigma, Buchs, Switzerland), Fe foil and Ni foil references were measured in transmission mode using ionization chamber detectors. Spectra were recorded on calcined powder samples, after pre-reduction (10 vol.% H_2/Ar, 800 °C, 15 h), as well as after reoxidation (20 vol.% O_2/Ar, 800 °C, 2 h).

Linear combination fitting (LCF) of Ni K-edge X-ray absorption near edge structure (XANES) spectra were performed in the spectral range -20 eV < E_0 < 30 eV around the absorption edge to quantify the fraction of each Ni species present in the samples. Reference compounds for each fit included Ni foil, NiO and calcined $La_{0.3}Sr_{0.55}Ti_{0.95}Ni_{0.05}O_{3\pm\delta}$ representing $Ni^{n+}{}_{oct}$ (n > 2) in the perovskite coordination.

4. Conclusions

Four transition metals (Cr, Fe, Mn and Mo) were screened for potential benefits towards the activity for the water gas shift (WGS) reaction and the stability improvement against sulfur poisoning of $La_{0.3}Sr_{0.55}TiO_{3\pm\delta}$ (LST) and $La_{0.3}Sr_{0.55}Ti_{0.95}Ni_{0.05}O_{3\pm\delta}$ (LSTN). While Cr, Mn and Mo impregnation on LST did not result in active catalysts, Fe exhibited significant WGS activity. Impregnation with Ni produced the most active catalysts. All other metals decreased the intrinsic activity of LSTN suggesting the presence of Ni/metal interactions. Sulfur stability compared to LSTN was improved only in the case of Fe-impregnated LSTN.

Implementing structural reversibility of Fe and Ni was attempted and both metals enhanced reciprocally their reduction behavior. Catalyst oxidation at 800 °C led to complete incorporation of Ni into the host perovskite, whereas Fe incorporation was found to be incomplete under these conditions and resulted in decreased catalyst redox stability at this temperature. Furthermore, WGS activity in the absence of sulfur was reduced compared to LSTN.

Although no beneficial consequences of bimetallic particle segregation were observed, the data demonstrate that Ni catalyst properties towards the WGS reaction at SOFC operation temperatures may be influenced significantly by the presence of other transition metals and that more than one metal can be segregated from LST-type host perovskites. However, the reincorporation behavior may be different for each metal, which has to be taken into account to exploit full structural reversibility of complex systems. Hence, further work is required to optimize regeneration conditions and to exploit the full potential of such materials.

Supplementary Materials: The following are available online at http://www.mdpi.com/2073-4344/9/4/332/s1. Figure S1: Ni speciation from a fit of XANES spectra, Figure S2: Ni K-edge XANES linear combination fit results, Figure S3: k^3-weighted χ(k) functions at the Ni K-edge, Figure S4: k^3-weighted χ(k) functions at the Fe K-edge, Table S1: sample list.

Author Contributions: All authors were involved in the conceptualization of this work. P.S. carried out the experiments, analyzed and interpreted the data and wrote the manuscript. D.B. synthesized and provided the perovskite-type materials. O.K. discussed results. A.H. and D.F. analyzed and interpreted the data and served as project leaders. D.F. contributed to writing the manuscript.

Funding: This research was funded by the Competence Center for Energy and Mobility (CCEM) and the Swiss National Science Foundation (SNF, No. 200021_159568).

Acknowledgments: The work was financially supported by the Competence Center for Energy and Mobility (CCEM), the Swiss National Science Foundation (SNF) and the Swiss Federal Office of Energy (SFOE). The work was conducted in the context of the Swiss Competence Center for Energy Research (SCCER BIOSWEET) of the Swiss innovation agency Innosuisse. The X10DA (SuperXAS) beamline at the Swiss Light Source (SLS) in Villigen (Switzerland) and M. Nachtegaal are thanked for kindly providing the beam time and support during measurements.

Conflicts of Interest: The authors declare no conflict of interest.

References

1. Nishihata, Y.; Mizuki, J.; Akao, T.; Tanaka, H.; Uenishi, M.; Kimura, M.; Okamoto, T.; Hamada, N. Self-regeneration of a Pd-perovskite catalyst for automotive emissions control. *Nature* **2002**, *418*, 164–167. [CrossRef]
2. Steiger, P.; Burnat, D.; Madi, H.; Mai, A.; Holzer, A.; Van Herle, J.; Kröcher, O.; Heel, A.; Ferri, D. Sulfur poisoning recovery on a solid oxide fuel cell anode material through reversible segregation of nickel. *Chem. Mater.* **2019**, *31*, 748–758. [CrossRef]
3. Steiger, P.; Nachtegaal, M.; Kröcher, O.; Ferri, D. Reversible segregation of Ni in $LaFe_{0.8}Ni_{0.2}O_3$ during coke removal. *ChemCatChem* **2018**, *10*, 4456–4464. [CrossRef]
4. Atkinson, A.; Barnett, S.; Gorte, R.J.; Irvine, J.T.S.; Mcevoy, A.J.; Mogensen, M.; Singhal, S.C.; Vohs, J. Advanced anodes for high-temperature fuel cells. *Nat. Mater.* **2004**, *3*, 17–27. [CrossRef]
5. McIntosh, S.; Gorte, R.J. Direct hydrocarbon solid oxide fuel cells. *Chem. Rev.* **2004**, *104*, 4845–4865. [CrossRef]
6. Granger, P.; Parvulescu, V.I. Catalytic NO_x abatement systems for mobile sources: From three-way to lean burn after-treatment technologies. *Chem. Rev.* **2011**, *111*, 3155–3207. [CrossRef]
7. Rostrup-Nielsen, J.R.; Pedersen, K. Sulfur poisoning of Boudouard and methanation reactions on nickel catalysts. *J. Catal.* **1979**, *59*, 395–404. [CrossRef]
8. Sehested, J. Four challenges for nickel steam-reforming catalysts. *Catal. Today* **2006**, *111*, 103–110. [CrossRef]
9. Strohm, J.J.; Zheng, J.; Song, C.S. Low-temperature steam reforming of jet fuel in the absence and presence of sulfur over Rh and Rh-Ni catalysts for fuel cells. *J. Catal.* **2006**, *238*, 309–320. [CrossRef]
10. Jahangiri, H.; Bennett, J.; Mahjoubi, P.; Wilson, K.; Gu, S. A review of advanced catalyst development for Fischer-Tropsch synthesis of hydrocarbons from biomass derived syn-gas. *Catal. Sci. Technol.* **2014**, *4*, 2210–2229. [CrossRef]
11. Quinn, R.; Dahl, T.A.; Toseland, B.A. An evaluation of synthesis gas contaminants as methanol synthesis catalyst poisons. *Appl. Catal. A* **2004**, *272*, 61–68. [CrossRef]
12. Boldrin, P.; Ruiz-Trejo, E.; Mermelstein, J.; Menendez, J.M.B.; Reina, T.R.; Brandon, N.P. Strategies for carbon and sulfur tolerant solid oxide fuel cell materials, incorporating lessons from heterogeneous catalysis. *Chem. Rev.* **2016**, *116*, 13633–13684. [CrossRef]
13. Wang, L.S.; Murata, K.; Inaba, M. Development of novel highly active and sulphur-tolerant catalysts for steam reforming of liquid hydrocarbons to produce hydrogen. *Appl. Catal. A* **2004**, *257*, 43–47. [CrossRef]
14. González, M.G.; Ponzi, E.N.; Ferretti, O.A.; Quincoces, C.E.; Marecot, P.; Barbier, J. Studies on H_2S adsorption and carbon deposition over Mo–Ni/Al_2O_3 catalysts. *Adsorpt. Sci. Technol.* **2000**, *18*, 541–550. [CrossRef]
15. Murata, K.; Saito, M.; Inaba, M.; Takahara, I. Hydrogen production by autothermal reforming of sulfur-containing hydrocarbons over re-modified Ni/Sr/ZrO_2 catalysts. *Appl. Catal. B* **2007**, *70*, 509–514. [CrossRef]
16. Rodriguez, J.A.; Hrbek, J. Interaction of sulfur with well-defined metal and oxide surfaces: Unraveling the mysteries behind catalyst poisoning and desulfurization. *Acc. Chem. Res.* **1999**, *32*, 719–728. [CrossRef]
17. L'Argentière, P.C.; Canon, M.G.; Figoli, N.S. XPS studies of the effect of Mn on Pd/Al_2O_3. *Appl. Surf. Sci.* **1995**, *89*, 63–68. [CrossRef]
18. Rodriguez, J.A.; Goodman, D.W. The nature of the metal-metal bond in bimetallic surfaces. *Science* **1992**, *257*, 897–903. [CrossRef]
19. Newsome, D.S. The water-gas shift reaction. *Catal. Rev.* **1980**, *21*, 275–318. [CrossRef]
20. Howald, R.A. The thermodynamics of tetrataenite and awaruite: A review of the Fe-Ni phase diagram. *Metall. Mater. Trans. A* **2003**, *34a*, 1759–1769. [CrossRef]
21. Massalski, T.B.; Perepezko, J.H.; Jaklovsky, J. Microstructural study of massive transformations in Fe-Ni system. *Mater. Sci. Eng.* **1975**, *18*, 193–198. [CrossRef]
22. Ratnasamy, C.; Wagner, J.P. Water-gas-shift catalysis. *Catal. Rev.* **2009**, *51*, 325–440. [CrossRef]
23. Steiger, P.; Delmelle, R.; Foppiano, D.; Holzer, L.; Heel, A.; Nachtegaal, M.; Kröcher, O.; Ferri, D. Structural reversibility and nickel particle stability in lanthanum iron nickel perovskite-type catalysts. *ChemSusChem* **2017**, *10*, 2505–2517. [CrossRef]
24. Steiger, P.; Alxneit, I.; Ferri, D. Nickel incorporation in perovskite-type metal oxides – implications on reducibility. *Acta Mater.* **2019**, *164*, 568–576. [CrossRef]

25. Sluchinskaya, I.A.; Lebedev, A.I.; Erko, A. Structural position and charge state of nickel in $SrTiO_3$. *Phys. Solid State* **2014**, *56*, 449–455. [CrossRef]
26. Beale, A.M.; Paul, M.; Sankar, G.; Oldman, R.J.; Catlow, C.R.A.; French, S.; Fowles, M. Combined experimental and computational modelling studies of the solubility of nickel in strontium titanate. *J. Mater. Chem.* **2009**, *19*, 4391–4400. [CrossRef]
27. Burnat, D.; Kontic, R.; Holzer, L.; Steiger, P.; Ferri, D.; Heel, A. Smart material concept: Reversible microstructural self-regeneration for catalytic applications. *J. Mater. Chem. A* **2016**, *4*, 11939–11948. [CrossRef]
28. Ravel, B.; Newville, M. Athena, Artemis, Hephaestus: Data analysis for X-ray absorption spectroscopy using ifeffit. *J. Synchrotron Radiat.* **2005**, *12*, 537–541. [CrossRef]